Received 28 September 2020; revised 8 November 2020; accepted 9 November 2020. Date of publication 16 November 2020; date of current version 15 January 2021.

Digital Object Identifier 10.1109/OJAP.2020.3037678

Sensor Arrangement in Monostatic Subsurface Radar Imaging

MARIA ANTONIA MAISTO [1,2], ROCCO PIERRI [1,2], AND RAFFAELE SOLIMENE [1,2] (Senior Member, IEEE)

[1]Dipartimento di Ingegneria, Universitá degli Studi della Campania - Luigi Vanvitelli, 81031 Aversa, Italy

[2]Consorzio Nazionale Interuniversitario per le Telecomunicazioni, 43124 Parma, Italy

CORRESPONDING AUTHOR: M. A. MAISTO (e-mail: mariaantonia.maisto@unicampania.it)

This work was supported by the Universitá della Campania Luigi Vanvitelli through Programma V:ALERE 2020, the project Efficient Probe pOsitioning for Near-fIeld Measurement techniques under Grant CUP: B66J20000680005.

ABSTRACT This article deals with microwave subsurface imaging achieved by inverting the linearized scattering operator. The focus is on the determination of a strategy for spatially sampling the data which allows to reduce the spatial data measurements and at the same time to keep the same achievable performance in the reconstructions. To this end, the measurement points are determined in order to approximate the point-spread function corresponding to the ideal continuous case (i.e., the case in which the data space is not sampled at all). For the sake of simplicity, the study is developed for a 2D scalar configuration. Also, the standard mono-static measurement arrangement is considered. However, in order to mimic a subsurface imaging scenario, a two-layered background medium is addressed. The main idea is to introduce suitable variable transformations which allow to express the point-spread functions as a Fourier-like transformation; this then provides insights for devising the sampling scheme. It is shown the resulting measurement spatial positions must be non-uniformly arranged across the measurement domain and their number can be much lower than the one provided by some commonly used literature sampling criteria.

INDEX TERMS Radar imaging, sampling, migration inversion.

I. INTRODUCTION

IN THIS article we address subsurface microwave imaging under a linearized scattering framework. Accordingly, the problem amounts to inverting the linearized scattering integral operator pertinent to a two-layered background medium. Moreover, data are assumed to be collected according to a monostatic strategy [1].

Regardless of the inversion method one may choose to employ, the scattering problem must be first translated into its finite dimensional counterpart through a suitable discretization process. This step is crucial and must be designed in order to trade-off different aspects of the problem. On the one hand, to keep the number of measurements as low as possible favourably affects the data acquisition time and the computational and the storage burden. On the other hand, the number and the way data are sampled impacts on the eigenspectrum of the matrix model arising from discretization and hence on the achievable performance and the resilience against noise and uncertainties [2].

The discretization step can be seen as a *sensor' selection* problem [3] which can be roughly stated as follows: given an $N \times M$ matrix model to be inverted, where N is the number of measurements and M the number of unknowns, select $L < N$ so that the achievable performance is optimized. The selection problem presents a combinatorial complexity and hence cannot be in practice addressed by an exhaustive exploration across all the possible measurement point arrangements. To overcome this drawback a number of methods based on convex optimization, greedy methods and heuristics have been developed in order to optimize the selection against some error metrics, such as the confidence

This work is licensed under a Creative Commons Attribution 4.0 License. For more information, see https://creativecommons.org/licenses/by/4.0/

ellipsoid, the mean square error [4], the frame potential [5], etc. Reference [6], [7], which are all linked to the singular values of the problem and try *to shape* their behavior [8]. All these methods are general purpose but require to run iterative procedures. Also, they usually require to a priori fix the number of measurements to be retained. The latter matter is of course connected to the Number of Degrees of Freedom (NDF) of the scattered field which can be used to estimate L [9], [10] and can also provide insights for sampling the field data [11].

The selection of the measurement points can be more specifically addressed by employing the properties of the kernel function of the scattering integral operator to be inverted and the related bandwidth arguments. In this case, no iterative procedures are required and the number of measurements to be employed in the reconstructions is the sampling points that fall within the measurement aperture and the adopted frequency band. For example, plane-wave expansion of the Green function, once evanescent waves are neglected, leads to a $\lambda/4$ spatial sampling step, with λ being the wavelength. Stationary phase arguments are employed in [12]–[15]; the resulting spatial sampling step depends on the extent of the spatial region to be imaged and is generally greater than $\lambda/4$ so to save many data points.

In view of the mentioned advantages provided by the sampling approach, this is the strategy adopted in this article to find the sensors' locations. In particular, we progress with respect to the results reported in [12], [13] by refining the theory upon which sampling is based. More in detail, the new sampling scheme is also able to take into account the spatially varying filtering introduced by the propagator in near-field configurations, the latter being usual in subsurface prospecting. In particular, it is shown that the sampling points must be non-uniformly arranged across the measurement domain according to a law that also depends on the dielectric permittivity of the half-space which models the subsurface scattering scenario. What is more, the number of the required points is generally lower than the one returned by previous approaches [12], [13].

The inverse problem related to subsurface imaging is ill-posed, or equivalently said, the singular values of the scattering operators tend to zero as their index increases [2]. Therefore, during the reconstruction some regularization scheme must be employed. Considering a finite number of measurements implicitly regularizes the inverse problem; indeed, the sensors' selection methods choose the measurements so as to *shape* the singular values in order to optimize some error metric. However, when L is large, it may happen that low singular values are retained and regularization is still necessary. Indeed, here is where the question of setting the number of measurements according to the NDF enters. This question is less important if the inverse operator is approximated by the adjoint one (i.e., adjoint based inversion). This is the case for migration inversion schemes which basically obtain the reconstructions by back-propagating the scattered field data according to the background Green

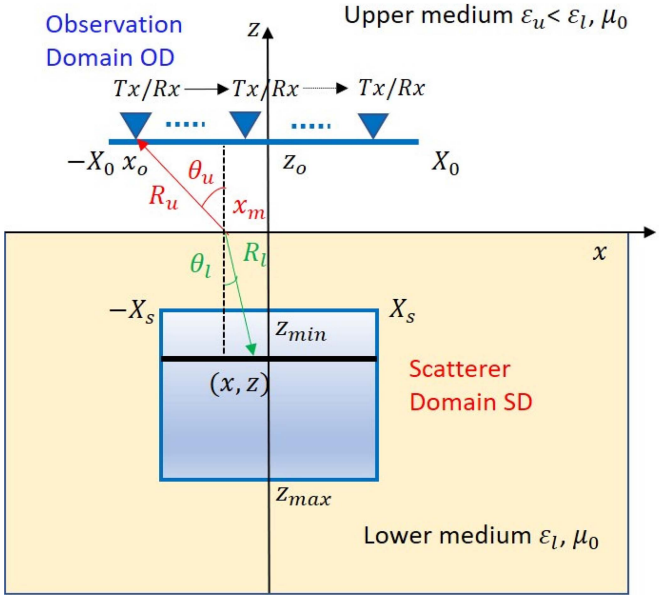

FIGURE 1. Geometry of the problem.

function [16], [17]. Indeed, by adjoint inversion, even a large L does not represent a serious issue since stability against the noise is implicitly obtained by the *filtering* imposed by the singular values themselves. However, the resulting reconstructions do not optimize some error metrics, for example they do not minimize the mean square error [17].

A common way to estimate the achievable performance, even by adjoint methods, is in terms of the point-spread function, which of course is related to the resolution that can be obtained in the reconstructions. Accordingly, in this manuscript, we derive the data sampling scheme in order to approximate the point-spread function corresponding to the continuous case, that is the ideal case in which data are not assumed to be sampled.

The rest of the paper is organized as follows. In Section II, the mathematical formulation of the problem is introduced. Section III is devoted to deriving the sampling scheme which is then checked by numerical examples in Section IV. In this section we consider the effect of the half-space dielectric permittivity as well. In particular, the case of free-space is also included and used as benchmark to better highlight the role of the subsurface scenario. Finally, conclusions are briefly reported. The paper also contains an appendix section where some mathematically details are reported.

II. PROBLEM DESCRIPTION

The study is developed for the 2D scalar scattering problem sketched in Fig. 1 with invariance assumed along the y-axis. The background medium consists of two homogeneous non-magnetic (i.e., the magnetic permeability is everywhere the same as that of the free-space μ_0) half-spaces separated by a planar interface at $z = 0$. In particular, the upper half-space is assumed to be the free-space and its dielectric permittivity is denoted by $\epsilon_u = \epsilon_0$; the lower one schematizes

the subsurface region and is electromagnetically denser with $\epsilon_l > \epsilon_0$.

The unknown targets are embedded in the lower half-space and assumed to reside within the rectangular region $SD = [z_{min}, z_{max}] \times [-X_s, X_s]$ (i.e., the scatterer domain). The incident field is radiated by an y-polarized line source of unitary amplitude at different frequencies within the wavenumber band $k_0 \in \Omega = [k_{0min}, k_{0max}]$, k_0 being the wavenumber in free-space. A monostatic configuration is considered, so that the scattered field is collected at the same position as the source while the latter can assume different positions across the measurement aperture. In particular, the measurement domain is assumed to be the segment $OD = [-X_0, X_0]$ of the x-axis located at the height $z_o \geq 0$. The case $z = 0$ corresponds to collecting the scattered field data just over the separation interface.

Under the Born approximation [18], the buried targets and the scattered field collected over $\Sigma = OD \times \Omega$ are linked through the following linear scattering operator

$$\mathcal{A} : \chi \in L^2(SD) \rightarrow E \in L^2(\Sigma) \tag{1}$$

where $L^2(SD)$ and $L^2(\Sigma)$ represent sets of square integrable functions supported over SD and Σ, respectively, $\chi(\boldsymbol{r}) = (\epsilon_s(\boldsymbol{r}) - \epsilon_l)/\epsilon_l$ is the so-called contrast function, with ϵ_s being the dielectric permittivity of the unknown scatterer.

The explicit form of the operator $\mathcal{A}$ is given as

$$E(x_o, k_0) = jk_l^2 \omega\mu_0 \int_{SD} G^2(x_o, \boldsymbol{r}, k_0)\chi(\boldsymbol{r})d\boldsymbol{r} \tag{2}$$

where ω is the angular frequency, $n = \sqrt{\epsilon_l/\epsilon_u}$ the refractive index and $k_l = nk_0$ the wavenumber in the lower half-space medium. The function $G(\cdot)$ is the Green function pertinent to the two-layered background medium and appears squared because of the considered mono-static configuration.

It is assumed that $|z_{min}| > \lambda_l$, λ_l being the wavelength in the lower half-space. Accordingly, the Green function in (2) can be approximated as [19]

$$G(x_o, \boldsymbol{r}, k_0) \approx \sqrt{h(x_o, \boldsymbol{r}, k_0)}e^{-jk_0\phi(x_o,\boldsymbol{r})} \tag{3}$$

where $\sqrt{h(x_o, \boldsymbol{r}, k_0)}$ takes into account the relevant amplitude factors, and $\phi(x_o, \boldsymbol{r}) = (R_u + nR_l)$ is the phase term that takes into account the propagation path. In particular, $\boldsymbol{r} = (x, y)$ and $\boldsymbol{r}_o = (x_o, z_o)$ are the target and the field points, and $R_u = \sqrt{(x_o - x_m(x_o, \boldsymbol{r}))^2 + z_o^2}$ and $R_l = \sqrt{(x_m(x_o, \boldsymbol{r}) - x)^2 + z^2}$ are the paths travelled by the waves in the upper and lower half-spaces, respectively, Finally, $x_m(x_o, \boldsymbol{r})$ is the refraction point at the half-spaces' interface which is given by the Snell's law as

$$\frac{x_o - x_m}{\sqrt{(x_o - x_m)^2 + z_o^2}} = n\frac{x_m - x}{\sqrt{(x_m - x)^2 + z^2}} \tag{4}$$

When the observation point is just located at the separation interface then $x_m = x_o$ and $z_o = 0$ so that the phase term simplifies as $\phi(x_o, \boldsymbol{r}) = nR_l$, with $R_l = \sqrt{x_o - x)^2 + z^2}$. Moreover, for the case of a homogeneous free-space background medium, the functions in (3) become $\sqrt{h(x_o, \boldsymbol{r}, k_0)} = -j\sqrt{\frac{j}{8\pi k_0 R}}$ and $\phi(x_o, \boldsymbol{r}) = R$, with $R(x_o, x, z) = \sqrt{(x_o - x)^2 + (z_o - z)^2}$.

In order to perform the reconstruction, equation (2) should be inverted for the χ function. In this article we choose to achieve inversion through the adjoint of the scattering operator, that is

$$\hat{\chi}(\boldsymbol{r}) = \left(\mathcal{A}^\dagger E\right)(\boldsymbol{r}) \tag{5}$$

with

$$\mathcal{A}^\dagger : E \in L^2(\Sigma) \rightarrow \chi \in L^2(SD) \tag{6}$$

being the adjoint of the scattering operator. This is a very common inversion strategy found in literature where it is addressed as migration, backpropagation, time-reversal and so on [20]–[22].

The point-spread function obtained by such an inversion scheme is the so-called model resolution kernel [23] which links the actual unknown to the reconstructed one, that is

$$\hat{\chi}(\boldsymbol{r}) = \int_{SD} d\boldsymbol{r}' psf(\boldsymbol{r}, \boldsymbol{r}')\chi(\boldsymbol{r}') \tag{7}$$

with

$$psf(\boldsymbol{r}, \boldsymbol{r}') = \int_\Sigma dk_0 dx_o A(x_o, \boldsymbol{r}, \boldsymbol{r}', k_0) \times e^{2jk_0[\phi(x_o,\boldsymbol{r}) - \phi(x_o,\boldsymbol{r}')]} \tag{8}$$

where $A(x_o, \boldsymbol{r}, \boldsymbol{r}', k_0) = [k_l^2\omega\mu_0]^2 h^*(x_o, \boldsymbol{r}, k_0)h(x_o, \boldsymbol{r}', k_0)$, with * denoting conjugation operator.

The previous formulation applies to the ideal cases where data are continuously collected over the frequency band and the measurement domain. Of course, practical scenarios require to discretize the problem by properly sampling the spatial and the frequency variables x_o and k_0. This aim is pursued in the next section where a sampling scheme is devised in order to approximate the point-spread function.

III. SAMPLING SCHEME

In this article we are mainly concerned with the determination of the spatial sampling. Therefore, the sampling of the wavenumber band is achieved by employing standard arguments based on the range extent of the area to be imaged, that is $\Delta k_0 = \pi/n(z_{max} - z_{min})$; denote as $k_{0l} = k_{0min} + (l-1)\Delta k_0$ the corresponding sampled frequencies. Hence, (8) is approximated as

$$psf(\boldsymbol{r}, \boldsymbol{r}') \approx \Delta k_0 \sum_l \int_{OD} dx_o A(x_o, \boldsymbol{r}, \boldsymbol{r}', k_{0l}) \times e^{2jk_{0l}[\phi(x_o,\boldsymbol{r}) - \phi(x_o,\boldsymbol{r}')]} \tag{9}$$

Now, in order to devise the spatial sampling we focus on the spatial integral appearing in the point-spread function expression (9), which for convenience is rewritten as follows

$$psf_{k_{0l}}(\boldsymbol{r}, \boldsymbol{r}') = \int_{OD} dx_o A(x_o, \boldsymbol{r}, \boldsymbol{r}', k_{0l}) \times e^{2jk_{0l}[\phi(x_o,\boldsymbol{r}) - \phi(x_o,\boldsymbol{r}')]} \tag{10}$$

where the frequency k_{0l} is considered as a parameter. In order to establish a sampling approximation that works for each frequency and for each positions within the investigation domain, in (10), we set $k_0 = k_{0max}$ and $z = z_{min}$. In particular, $z = z_{min}$ is the most critical case for discrete point-spread function approximation since the scattered field arising from targets that are closer to the observation domain has a larger spatial bandwidth and hence requires more samples for a good point-spread function approximation. Accordingly, (10) is particularized as

$$psf_{k_{0max}}(x, x') = \int_{OD} dx_o A\big(x_o, x, x', k_{0max}\big) \times e^{2jk_{0max}[\phi(x_o,x)-\phi(x_o,x')]} \quad (11)$$

where the dependence on z has been understood since it was set at the constant value z_{min}.

The next step is to rewrite $psf_{k_{0max}}$ so that Fourier based arguments can be used to gain insights on the spatial sampling. To this end, we basically adapt the developments and tools presented in [24], [25] to the problem at hand.

More in detail, we first introduce a transformation $\eta : x \in [-X_s, X_s] \rightarrow \eta(x) \in [\eta(-X_s), \eta(X_s)]$ that basically stretches the interval $[-X_s, X_s]$ into $[\eta(-X_s), \eta(X_s)]$. At this juncture, such a function does not need to be defined yet and its usefulness will be clear later on. What is important is that $\eta(x)$ is monotonic with $\frac{d\eta}{dx} > 0$.

Then, by employing the first order integral form of the Taylor remainder, the phase term is rewritten as

$$2k_{0max}\big[\phi(x_o, x) - \phi\big(x_o, x'\big]\big) = k_{0max}(\eta_2 - \eta_1)w(\eta_2, \eta_1, x_o) \quad (12)$$

with

$$w(\eta_2, \eta_1, x_o) = 2\int_0^1 \frac{\partial\phi(x_o, x(\eta))}{\partial\eta}\bigg|_{\eta=\eta_1+v(\eta_2-\eta_1)} dv \quad (13)$$

and $\eta_2 = \eta(x)$ and $\eta_1 = \eta(x')$. The function $w(\eta_2, \eta_1, x_o)$ is continuous and monotonic decreasing with respect to x_o (hence invertible) $\forall\eta_2, \eta_1$ (see Appendix for some details). This allows to replace the integration in x_o with the integration in w. In particular, on denoting

$$\Omega w(\eta_2, \eta_1, X_0) = \frac{w(\eta_2, \eta_1, -X_0) - w(\eta_2, \eta_1, X_0)}{2} \quad (14)$$

and

$$w_{avg}(\eta_2, \eta_1, X_0) = \frac{w(\eta_2, \eta_1, -X_0) + w(\eta_2, \eta_1, X_0)}{2} \quad (15)$$

and by setting $w = \bar{w} + w_{avg}$, expression (10) can be rewritten as

$$psf_{k_{0max}}(\eta_2, \eta_1) = e^{jk_{0max}w_{avg}[\eta_2-\eta_1]} \times \int_{-\Omega w}^{\Omega w} K(\bar{w}, \eta_2, \eta_1, k_{0max}) \times e^{jk_{0max}\bar{w}[\eta_2-\eta_1]} d\bar{w} \quad (16)$$

where $K(\bar{w}, \eta_2, \eta_1, k_{0max}) = -A(x_o(\bar{w}), \eta_2, \eta_1, k_{0max})\frac{dx_o}{d\bar{w}}$. Note that, for the sake of notation simplicity, we omitted to explicitly report the dependence on η_2 and η_1 of Ωw and w_{avg}. However, this dependence is indicated in (14) and (15) and highlights the spatially varying behaviour of the point-spread function which, as opposed to far-field configurations, is a characteristic feature of near-field configurations.

At this point, in order to simplify the matter a little bit, the transformation $\eta(x)$ is conveniently set as [24]

$$\eta(x) = \phi(-X_0, x) - \phi(X_0, x) \quad (17)$$

This way, the point-spread function bandwidth Ωw is made constant and equal to 1 (see Appendix for the details) so that the spatially varying behaviour mentioned above results now encoded into the non-linear link between the variables x and η, which clearly implies a spatially varying resolution. Also, by noting that the leading order contribution in (16) occurs for $\eta_2 - \eta_1 = 0$ [26], the amplitude factor is approximated as $K(\bar{w}, \eta_2, \eta_1, k_0) \approx K(\bar{w}, \eta_1, \eta_1, k_0) = K(\bar{w}, \eta_1, k_0)$. Accordingly, (16) becomes

$$psf_{k_{0max}}(\eta_2, \eta_1) \simeq e^{jk_{0max}w_{avg}[\eta_2-\eta_1]} \int_{-1}^{1} K(\bar{w}, \eta_1, k_{0max}) \times e^{jk_{0max}\bar{w}[\eta_2-\eta_1]} d\bar{w} \quad (18)$$

Now, (18) resembles a Fourier transformation that can be approximated by assuming to collect data over a set of spatial positions so that $\bar{w}$ results uniformly sampled. Say $\Delta\bar{w} = \Delta w$ the corresponding sampling step and $\bar{w}_m$ the corresponding sampling points, then

$$psf_{k_{0max}}(\eta_2, \eta_1) \simeq e^{jk_{0max}w_{avg}[\eta_2-\eta_1]}\Delta w \times \sum_m K\big(\bar{w}_m, \eta', k_{0max}\big)e^{jk_{0max}\bar{w}_m[\eta_2-\eta_1]} \quad (19)$$

Hence, standard Fourier arguments, as the one invoked for avoiding grating lobes in array antenna theory, suggest that the sampling step for $\bar{w}$ should be

$$\Delta w(\eta_2, \eta_1) \leq \frac{2\pi}{k_{0max}(\eta(X_s) - \eta(-X_s))} = \frac{\pi}{k_{0max}\eta(X_s)}. \quad (20)$$

where the outer right hand side term arises because $\eta(-X_s) = -\eta(X_s)$. More specifically, by highlighting $\bar{w}_m$ in terms of the corresponding sampling points in x_o, i.e., x_{om}, (20) rewrites as

$$w(\eta_2, \eta_1, x_{om+1}) - w(\eta_2, \eta_1, x_{om}) \leq \frac{\pi}{k_{0max}\eta(X_s)} \quad (21)$$

with $x_{om+1} < x_{om}$. Eq. (21) can be used to determine the spatial sample positions. In particular, (21) dictates that the sampling points change with η_2 and η_1 and are in general non-symmetric with respect to the centre of the measurement aperture. Since it is natural to look for a symmetric measurement point deployment, we consider $\eta_2 = -\eta_1$. Accordingly, (21) particularizes as

$$w(\eta, -\eta, x_{om+1}) - w(\eta, -\eta, x_{om}) = \frac{\pi}{k_{0max}\eta(X_s)} \quad (22)$$

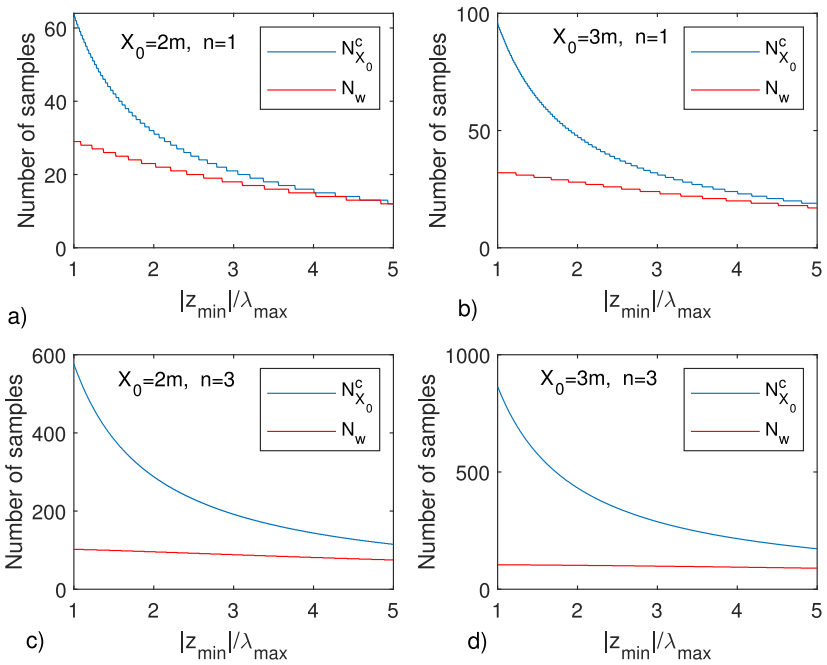

FIGURE 2. Comparison between N_W and $N^c_{X_0}$ as a function of $|z_{min}|$ for two different values of X_0 and n and $z_O = 0$, $X_S = 1.5$m and $\lambda_{max} = 1m$.

with $\eta = \eta_2 = -\eta_1$, from which eventually the equation for finding the sampling points x_{om} arises as (see Appendix)

$$\phi(x_{om}, -x) - \phi(x_{om}, x) = \frac{m\pi\,\eta(x)}{k_{0max}\eta(X_s)} \tag{23}$$

Eq. (23) still entails that the sampling points are dependent on x (i.e., $\eta(x)$). More in detail, through a direct solution of (23) for x_{om}, it can be shown that the lower x the more the sampling points tend to accumulate around $x_o = 0$. Therefore, in order to have a better coverage of the measurement line, in (23) we set $x = X_s$ (the largest value allowed by the transverse size of SD). Therefore, eventually the sampling point equation that we use is the following

$$\phi(x_{om}, -X_s) - \phi(x_{om}, X_s) = \frac{m\pi}{\alpha_{OS}k_{0max}} \tag{24}$$

where α_{OS} is an oversampling factor. At this juncture we have to point out that, when the sampling points x_{om} are obtained from (24), eq. (21) is not necessarily verified for all η_2, η_1. In general, an oversampling factor could be required. A slight oversampling is also required in order to avoid the point-spread function side-lobes start to increase for some target positions which are close to the transverse boundaries (i.e., $x = \pm X_s$). This is particularly true for small relative bandwidths. For large bandwidths, having set the sampling step in correspondence of k_{max}, guarantees a certain degree of oversampling for most frequencies. In the sequel we considered a slight oversampling factor of $\alpha_{OS} = 1.1$. Accordingly, the required number of spatial samples (to be deployed non-uniformly, though symmetrically) turns to be

$$N_w = \frac{2\Omega w}{\Delta w} = \frac{2k_{0max}\alpha_{OS}\eta(X_s)}{\pi}$$

that, for homogeneous scenario, becomes

$$N_w = \frac{4\alpha_{OS}}{\lambda_{min}}[R(-X_0, X_s, z_{min}) - R(X_0, X_s, z_{min})] \tag{25}$$

and for the half-space case

$$N_w = \frac{4\alpha_{OS}}{\lambda_{min}}[R_u(-X_0, X_s, z_{min}) - R_u(X_0, X_s, z_{min}) + nR_l(-X_0, X_s, z_{min}) - nR_l(X_0, X_s, z_{min})] \tag{26}$$

It is interesting to compare N_w with some commonly used literature results. To this end, we consider the estimation reported in [12], [13]. In particular, those studies refer to a free-space configuration. Accordingly, the comparison is pursued only for the case of homogeneous scenario or for $z_o = 0$ (where, for the sampling point estimation, the background medium can be assumed as being homogeneous and equal to the lower half-space). In [12], [13] two sampling criteria were suggested. One, which besides the configuration parameters (frequency, SD size, its distance from the observation line), also depends on the measurement aperture; and another one from which, after *signal compression*, such a dependence is removed. The second one requires fewer spatial samples, that is

$$N^c_{x_o} = \frac{8X_0X_s}{\lambda_{min}z_{min}} \tag{27}$$

and hence it has been selected as benchmark for our sampling scheme (which in any case does not require *signal compression*). It can be easily shown that, for fixed X_0 and X_s, $N_w \leq N^c_{x_o}$ with equality tending to be reached when $|z_o - z_{min}|$ increases; for fixed $|z_o - z_{min}|$ and increasing X_0, N_w

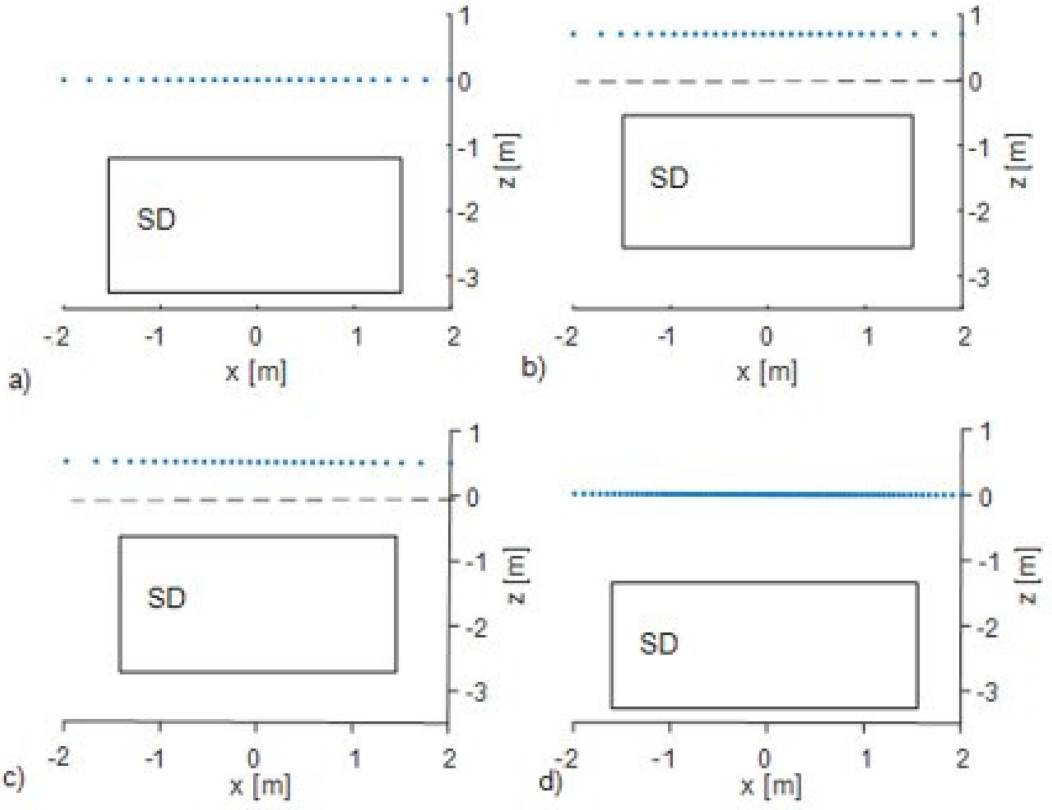

FIGURE 3. Schematic representation of the geometrical parameters of the considered scattering configurations and sampling point locations for $k_{0min} = 2\pi\, m^{-1}$, $k_{0max} = 5.337\pi\, m^{-1}$ $X_S = 1.5m$ and $X_0 = 2m$. Figure a) refers to scattering scenario 1 with $z_O = 0$, $z_{min} = -1.2m$, $z_{max} = -3.2m$; the corresponding number of samples are $N_W = 29$ and $N^c_{x_O} = 54$. Figures b) and c) refer to scattering scenario 2, the dashed line is where the interface is located and $n = 3$. In particular in b) $z_O = 0.7m$, $z_{min} = -0.5m$, $z_{max} = -2.5m$ and the sampling points are $N_W = 32$, whereas for c) $z_O = 0.5m$, $z_{min} = -0.7m$, $z_{max} = -2.7m$ and $N_W = 33$. Finally, figure d) refers to scattering scenario 3 with $n = 3$, $z_O = 0$, $z_{min} = -1.2m$, $z_{max} = -3.2m$, $N_W = 85$ and $N^c_{x_O} = 160$. Note that in this case the interface has not been highlighted since it coincides with the measurement line.

grows more slowly than $N^c_{x_o}$. This comparison is graphically illustrated in Fig. 2. It is clearly seen that $N^c_{x_o}$ is generally much larger than N_w and that this is enhanced as n increases. If T is the time required for collecting data at a fixed spatial position, then the time saved by the new sampling scheme grows with the linear law $(N^c_{X_O} - N_w)T$. Hence, it can be concluded that the proposed spatial sampling scheme proves to be more effective for near-zone configurations.

IV. NUMERICAL ANALYSIS

In this section we present a few numerical examples in order to check the sampling scheme introduced above. In particular, eq. (7) shows that the reconstruction is basically a filtered version of the actual unknown, with the filtering dictated by the point-spread features. As a consequence, in order to compare the reconstructions returned by the two sampling schemes, we focus on the comparison between the 'exact' point-spread function *psf* and the one obtained by employing the sampling scheme in (24), psf_e. In particular, in order to obtain the two point-spread functions, we consider the reconstruction of a point-like target whose contrast function is defined as $\chi = \delta(\mathrm{r} - \mathrm{r'})$, with $\mathrm{r'} \in SD$. More in detail, by exact point-spread function *psf* we mean (8) numerically implemented by employing a very fine and uniform grid of points within the data space Σ; psf_e takes into account the proposed sampling strategy and is still obtained by implementing (8) but the spatial points are non-uniformly deployed according to (24). In particular, according to the formulation introduced in Section III, in this case the point-spread function is computed as

$$psf_e(\boldsymbol{r}, \boldsymbol{r}') = \sum_{m,l} e^{jk_{0l} w_{avg}[\eta(\boldsymbol{r}) - \eta(\boldsymbol{r}')]} \Delta w \Delta k_0 \times K\left(\bar{w}_m, \eta(\boldsymbol{r}'), k_{0l}\right) e^{jk_{0l}\bar{w}_m[\eta(\boldsymbol{r}) - \eta(\boldsymbol{r}')]} \quad (28)$$

It must be noted that, while in Section III η was highlighted as a function of only x because z was set at z_{min} (i.e., the most critical case for sampling), here, η turns out to be dependent on x and z.

As a final remark before addressing the numerical examples, we advise the reader that in the following, the approximate Green function introduced in Section II is not exploited. Indeed, the Green function is computed by using its plane-wave expansion (Weyl expansion) [18].

The numerical examples deals basically with three scattering scenarios: the free-space case (scenario 1), the half-space case with measurements taken away from the separation

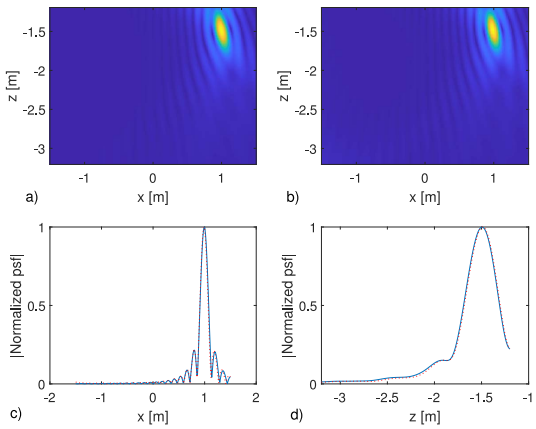

(a) Corresponds to a) in Fig. 3, $|C(\boldsymbol{r}')| = 0.99$.

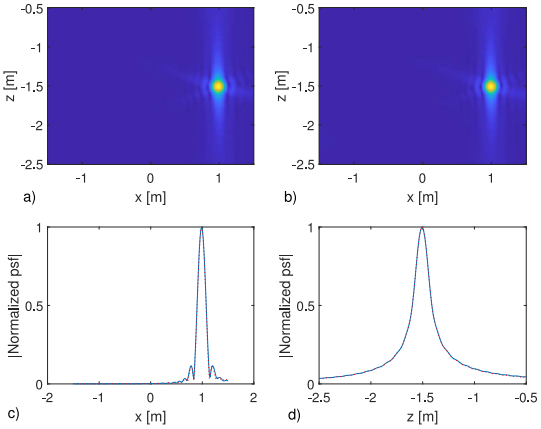

(b) Corresponds to b) of Fig. 3, $|C(\boldsymbol{r}')| = 0.99$.

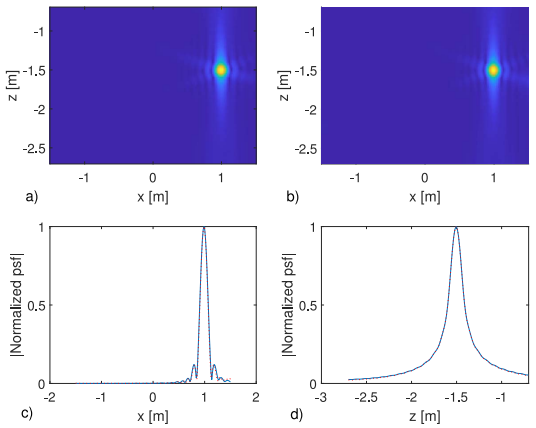

(c) Corresponds to c) of Fig. 3, $|C(\boldsymbol{r}')| = 0.99$.

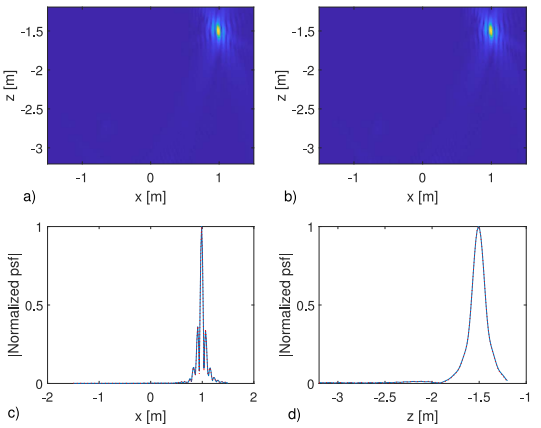

(d) Corresponds to d) of Fig. 3, $|C(\boldsymbol{r}')| = 0.99$.

FIGURE 4. **Illustrating the normalized point-spread function amplitudes for a point target located at $(x', z') = (1, -1.5)m$. Each panel refers to the analogous reported in Fig. 3 and shows the point-spread function and its cut-views. The 'exact' point-spread functions are denoted by blue solid lines whereas the ones obtained using the proposed sampling scheme by dotted red lines.**

interface (scenario 2) and the half-space case with measurements just collected over the separation interface (scenario 3). In particular, the free-space case is addressed in order to have a reference for the subsurface configuration. Also, it allows an easy vis a vis comparison for the estimation of the required number of samples reported in [13], which has been indeed worked out for such a case. Of course, $N^c_{x_o}$ can be generalized to the half-space case. In particular, for the case the scattered field is observed just over the separation interface, the number of samples is computed by using the wavenumber of the lower half-space as the scattering phenomenon were taking place in a homogeneous medium. However, for the case of the stand off configuration we did not pursue the generalization of $N^c_{x_o}$.

We start by showing in Fig. 3 the number and the spatial measurement deployment across the measurement line $[-X_0, X_0] = [-2, 2]m$ for the scattering scenarios whose details are provided in the caption. Note that in all the cases, the sizes of OD and SD as well as $|z_o - z_{min}|$ are kept constant. This allows to highlight the role played by the background medium. More in detail, panels b) and c) both address the case of scenario 2 but with a different stand off distance from the interface, whereas panel a) and d) refer to scattering scenarios 1 and 3, respectively. From such a figure the expected non-uniform sensor arrangement can be appreciated. Moreover, N_w results much lower than $N^c_{x_o}$ (see panels a) and d) for which the comparison has been pursued). Also, it can be noted that the required spatial samples increase while moving from case a) to case d). This indeed could be expected since this is somehow like passing from free-space to a denser medium corresponding to the lower half-space. In Fig. 4 the normalized point-spread functions corresponding to the cases depicted in Fig. 3 are shown. As can be seen, while moving towards the case relative to scenario 3, the main beam of the point-spread function tends to become narrower. This entails an improvement of the achievable resolution. This is a very well known fact

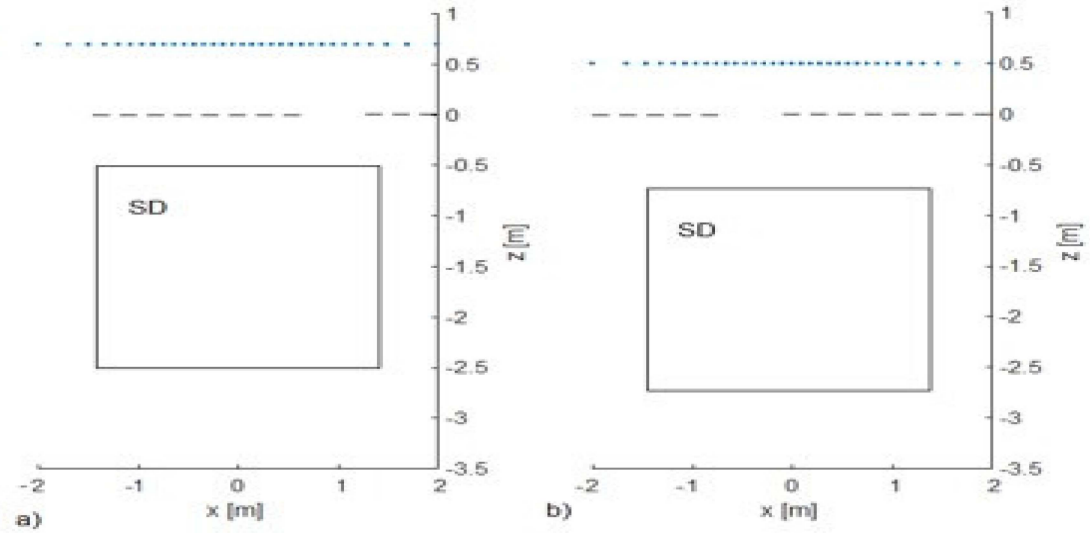

FIGURE 5. Schematic representation of the geometrical parameters and sampling point locations for the scattering scenario 2 for $k_{0min} = 2\pi\, m^{-1}$, $k_{0max} = 5.337\pi\, m^{-1}$ $X_S = 1.5m$ and $X_0 = 2m$ but $n = 6$. In particular, in a) $z_O = 0.7m$, $z_{min} = -0.5m$, $z_{max} = -2.5m$ and the sampling points are $N_W = 32$, whereas for b) $z_O = 0.5m$, $z_{min} = -0.7m$, $z_{max} = -2.7m$ and $N_W = 33$. The dashed line is where the interface is located.

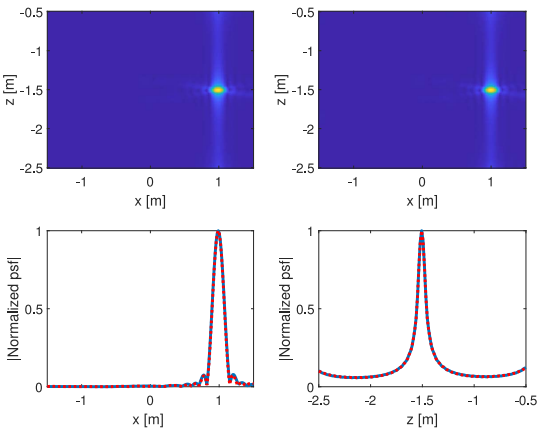

(a) Corresponds to a) in Fig. 5, $|C(\boldsymbol{r}')| = 0.99$.

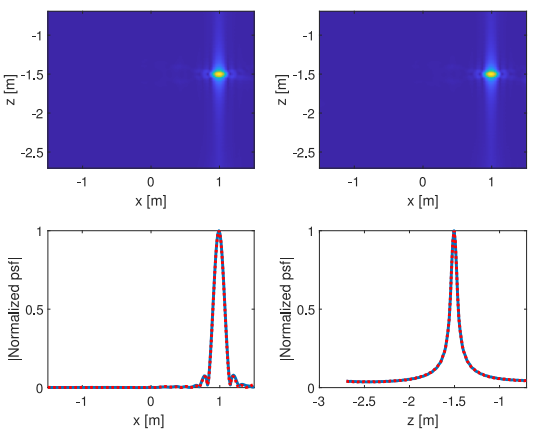

(b) Corresponds to b) of Fig. 5, $|C(\boldsymbol{r}')| = 0.99$.

FIGURE 6. Illustrating the normalized point-spread function amplitudes for a point target located at $(\boldsymbol{x}', \boldsymbol{z}') = (1, -1.5)m$. Each panel refers to the analogous reported in Fig. 5 and shows the point-spread function and its cut-views. The 'exact' point-spread functions are denoted by blue solid lines whereas the ones obtained using the proposed sampling scheme by dotted red lines.

and it is consistent with the higher number of samples that are required. A detailed estimation of how the half-space configuration parameters affect resolution has been reported in [27]. Here, what matters is that the exact point-spread function and the one returned by (28) practically overlap. This is quantified by the correlation coefficient

$$C(\boldsymbol{r}') = \frac{\int_{SD} psf_e(\boldsymbol{r}, \boldsymbol{r}') psf^*(\boldsymbol{r}, \boldsymbol{r}') d\boldsymbol{r}}{\|psf_e\|(\boldsymbol{r}')\|psf\|(\boldsymbol{r}')} \tag{29}$$

where $\|psf_e\|(\boldsymbol{r}')$ and $\|psf\|(\boldsymbol{r}')$ are the norms computed with respect to $\boldsymbol{r}$ and hence remains function of $\boldsymbol{r}'$. Such a parameter is reported in each sub-panel of Fig. 3 and, as can be seen, it is always very high (i.e., > 0.9). This means that the estimated number of samples works very well for estimating the point spread function. What is more, this holds true even though N_w is lower than $N^c_{x_o}$.

In order to inspect how the dielectric permittivity affects the sampling points and the resolution we now change the refractive index. In particular, for the case of scenario 3 it is readily seen from eqs. (25) and (26) that the number of samples grows linearly with n. Therefore, we just consider scenario 2. In particular, the same two examples as before are re-run with a refractive index $n = 6$ and the corresponding results are shown in Figs. 5 and 6(c). In particular, the first figure shows the sampling point locations whereas Fig. 6(c) report the point-spread functions. As can be seen from 5, by increasing n, N_w and the distribution of the sampling points do not change significantly (as opposed to case relative to scenario 3). On contrary, as expected, the number of required frequencies increases from 20 to 40. As far as the resolution is concerned, while transverse resolution remains practically unchanged, resolution along the range improves (see

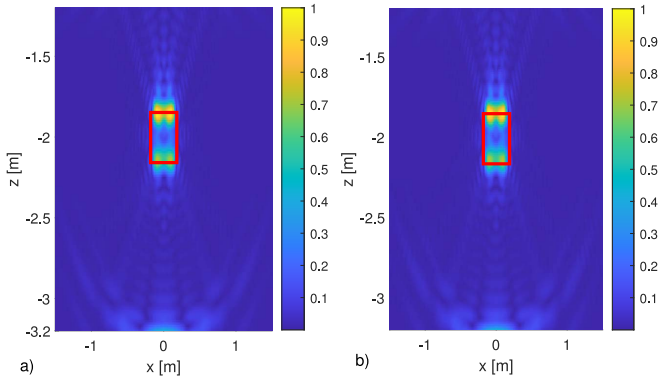

FIGURE 7. Normalized reconstruction of a $30 \times 30cm$ square scatterer with dielectric permittivity $\epsilon_S = 11\epsilon_0$ and centered in $(0, -2)m$. The scattering scenario is the same as the panel d) in Fig. 3. In panel a), the reconstruction is obtained by collecting $N^c_{x_O} = 160$ measurements arranged uniformly (as suggested in [13]), in b) $N_W = 80$ measurements are collected as shown in the panel d) of Fig. 3. The red lines border the actual scatterer shape.

Fig. 6(c)). This example suggests that for stand-off distance the lower half-space permittivity mainly affects range resolution and the number of required frequencies. Of course, this effect *quantitatively* depends on the geometrical parameters of the configuration (i.e., OD, SD and $|z_o - z_{in}|$). However, again, the proposed sampling scheme works very well in estimating the point-spread function. Accordingly, the proposed theoretical framework allows to foresee what is going on when the configuration parameters have been set.

Finally, we end this section by comparing the proposed strategy with the one suggested in [13] for a reconstruction example. In particular, scattering scenario 3, as in Fig. 3, is considered whereas the scatterer is a dielectric square $30 \times 30cm^2$ in size, with dielectric permittivity $\epsilon_s = 11\epsilon_0$ and centered at $(0, -2)m$. Fig. 7 shows the corresponding reconstruction results: the left panel refers to the reconstruction obtained by collecting the field as suggested in [13], the right one to the proposed non-uniform sampling scheme. As expected, due to the adopted linear inversion, only a qualitative reconstruction of the target is obtained. In fact, only the scatterer's "discontinuities" along the z axes are clearly distinguishable due to the "high-pass" filtering introduced by the reconstruction algorithm, which is typical of a reflection mode configuration. However, what matters here is that, in spite of the reduction of the measurement number (from $N^c_{x_o} = 160$ to $N_w = 80$), the proposed sampling strategy allows to obtain a reconstruction which is practically the same as the ones returned by using the denser sampling in [13].

V. CONCLUSION

In this contribution, we have addressed the problem of devising a sampling scheme in order to collect the data to be used in a migration-like reconstruction scheme for subsurface prospecting. To this end, thanks to suitable variable transformations, the corresponding point-spread function has been recast as a Fourier-like transformation which then suggested the spatial sampling strategy. Instead, frequencies have been sampled according to a standard criterion.

It has been shown that the resulting spatial sampling points are to be non-uniformly arranged across the measurement aperture. Also, the required number of spatial samples is usually lower than the one dictated by commonly used literature results. This being a remarkable advantage since it allows to use fewer sensors for real aperture radar systems or to reduce the time for data collection in synthetic aperture radar systems. A few numerical examples confirmed the goodness of the proposed sampling scheme. Also, the role of the dielectric permittivity of the lower half-space schematizing the subsurface scattering scenario has been highlighted. As expected, compared to the homogeneous free-space case, more spatial points are needed and they must be placed in general on different positions (with respect to the free-space case), according to the medium's dielectric permittivity.

In view of the obtained promising results, extension of the theory to more involved cases is currently under development. In particular, these further developments concern the full $3D$ case as well as background media consisting of more layers [28], [29].

Related to the sampling there is, of course, the question of the achievable resolution. Indeed, configurations that allow for better resolution (i.e., point-spread function having narrower main beam) require a denser sampling. This has been clearly verified in the reported numerical examples. Nonetheless, we did not thoroughly addressed this point in the paper since the focus was on the sampling scheme. A detailed study of the achievable resolution and related closed-form estimation for the half-space configuration was reported in [27].

APPENDIX

This appendix is devoted to providing some mathematical details that for the sake of readability have been omitted in the previous sections.

Derivation of eq. 12: Consider the phase term in (11), that is

$$2\left[\phi(x_o, x) - \phi\left(x_o, x'\right)\right] = 2[\phi(x_o, x(\eta_2)) - \phi(x_o, x(\eta_1))] \tag{30}$$

Then, by using the Fundamental Theorem of Calculus (FTC), (30) can be rewritten as

$$2\left[\phi(x_o, x) - \phi\left(x_o, x'\right)\right] = 2\int_0^1 \frac{\partial}{\partial \nu}\phi(x_o, x(\eta))|_{\eta=\eta_1+\nu(\eta_2-\eta_1)}d\nu \tag{31}$$

which is basically the integral form of the first order Taylor series remainder. Now, eqs. (12) and (13) simply arise on applying the chain rule for differentiation, that is

$$\begin{aligned} &2\left[\phi(x_o, x) - \phi\left(x_o, x'\right)\right] \\ &\quad = 2(\eta_2 - \eta_1) \times \int_0^1 \frac{\partial}{\partial \eta}\phi(x_o, x(\eta))|_{\eta=\eta_1+\nu(\eta_2-\eta_1)}d\nu \end{aligned} \tag{32}$$

Invertibility of w with respect to x_o: This can be easily shown by direct calculation. To this end, we need first to express $\frac{\partial}{\partial\eta}\phi(x_o, x(\eta))$. By recalling that $\phi(x_o, x(\eta)) = R_u[x_o, x_m(x_o, x(\eta))] + nR_l[x_m(x_o, x(\eta)), x)]$, it is obtained that

$$\frac{\partial}{\partial\eta}\phi(x_o, x(\eta)) = \frac{\partial R_u}{\partial x_m}\frac{\partial x_m}{\partial x}\frac{dx}{d\eta} + n\left[\frac{\partial R_l}{\partial x_m}\frac{\partial x_m}{\partial x}\frac{dx}{d\eta} + \frac{\partial R_l}{\partial x}\frac{dx}{d\eta}\right] \tag{33}$$

which can be more conveniently rewritten as

$$\frac{\partial}{\partial\eta}\phi(x_o, x(\eta)) = -\left(\hat{x}\cdot\hat{R}_u + n\hat{x}\cdot\hat{R}_l\right)\frac{\partial x_m}{\partial x}\frac{dx}{d\eta} + n\hat{x}\cdot\hat{R}_l\frac{dx}{d\eta} \tag{34}$$

where $\hat{x}$, $\hat{R}_u$ and $\hat{R}_l$ are unitary direction vectors (see Fig. 1) and $\cdot$ denotes the scalar product. In particular, for $x_o < x$, $\hat{R}_u = (-\sin\theta_u, \cos\theta_u)$ and $\hat{R}_l = (\sin\theta_l, -\cos\theta_l)$, whereas for $x_o > x$, $\hat{R}_u = (\sin\theta_u, \cos\theta_u)$ and $\hat{R}_l = (-\sin\theta_l, -\cos\theta_l)$. Hence, because of the Snell's law $\sin\theta_u = n\sin\theta_l$, (34) simplifies as

$$\frac{\partial}{\partial\eta}\phi(x_o, x(\eta)) = n\hat{x}\cdot\hat{R}_l\frac{dx}{d\eta} \tag{35}$$

Now, in order to show that $w(\eta_2, \eta_1, x_o)$ is monotonically decreasing it is sufficient to check that $w(\eta_2, \eta_1, x_{o2}) - w(\eta_2, \eta_1, x_{o1}) < 0$ when $x_{o2} > x_{o1}$ and $\forall\eta_1, \eta_2$. According to (35) and the definition (12), such a difference can be expressed as

$$2n\int_0^1 \hat{x}\cdot\left(\hat{R}_l(x_{o2}, x(\eta)) - \hat{R}_l(x_{o1}, x(\eta))\frac{dx}{d\eta}|_{\eta=\eta_1+\nu(\eta_2-\eta_1)}d\nu\right. \tag{36}$$

It can be easily verified that when $x_{o2} > x_{o1}$, $\hat{x}\cdot(\hat{R}_l(x_{o2}, x(\eta)) - \hat{R}_l(x_{o1}, x(\eta))$ is a real negative function of η. Hence, by recalling that (by construction) $dx/d\eta > 0$, then the integral (36) is always negative. This proves the monotonic behaviour of w with respect to x_o.

Invertibility of η with respect to x: With reference to the transformation introduced in (17), to show that $\eta(x)$ is an increasing monotonic function we have to prove that $d\eta/dx > 0$. More in detail,

$$\frac{d\eta}{dx}(x) = \frac{\partial\phi(-X_0, x)}{\partial x} - \frac{\partial\phi(X_0, x)}{\partial x} \tag{37}$$

which, upon employing (35), can be rewritten as

$$\frac{d\eta}{dx}(x) = n\left(\hat{x}\cdot\hat{R}_l(-X_0, x) - \hat{x}\cdot\hat{R}_l(X_0, x)\right) \tag{38}$$

from which, by employing the same geometrical arguments exploited right above, one can conclude that $d\eta/dx > 0$.

Expression of the bandwidth Ωw: According to (14), the bandwidth can be expressed as

$$\Omega w(\eta_2, \eta_1, X_0) = \int_0^1 \frac{\partial}{\partial\eta}[\phi(-X_0, x(\eta)) - \phi(X_0, x(\eta))]|_{\eta=\eta_1+\nu(\eta_2-\eta_1)}d\nu \tag{39}$$

with

$$\frac{\partial}{\partial\eta}[\phi(-X_0, x(\eta)) - \phi(X_0, x(\eta))] = \frac{\partial}{\partial x}[\phi(-X_0, x(\eta)) - \phi(X_0, x(\eta))]\frac{dx}{d\eta} = 1 \ \ \forall\eta \tag{40}$$

where $\eta(x)$ defined in (17) has been employed. Accordingly, (39) says that $\Omega w = 1\ \forall\eta_2, \eta_1$.

Derivation of the sample point equation (22): We start by considering eq. (22), which here is rewritten for convenience

$$w(\eta(x), \eta(-x), x_{om+1}) - w(\eta(x), \eta(-x), x_{om}) = \frac{\pi}{k_{0max}\eta(X_s)} \tag{41}$$

Now, by exploiting eq. (12), eq. (41) is rewritten as

$$\phi(x_{om+1}, -x) - \phi(x_{om+1}, x) - \phi(x_{om}, -x) + \phi(x_{om}, x)] = \frac{\pi\eta(x)}{k_{0max}\eta(Xs)} \tag{42}$$

where it has been considered that $\eta(-x) = -\eta(x)$. Hence, (23) follows.

ACKNOWLEDGMENT

The authors kindly thank Giuseppina Nuzzo for proofreading the manuscript.

REFERENCES

[1] M. Soumekh, *Synthetic Aperture Radar Signal Processing With MATLAB Algorithms*. New York, NY, USA: Wiley, 1999.
[2] M. Bertero, "Linear inverse and ill-posed problems," *Adv. Electron. Electron Phys.*, vol. 75, pp. 1–120, 1989.
[3] S. J. Reeves and L. P. Heck, "Selection of observations in signal reconstruction," *IEEE Trans. Signal Process.*, vol. 43, no. 3, pp. 788–791, Mar. 1995.
[4] S. Joshi and S. Boyd, "Sensor selection via convex optimization," *IEEE Trans. Signal Process.*, vol. 57, no. 2, pp. 451–462, Feb. 2009.
[5] J. Ranieri, A. Chebira, and M. Vetterli, "Near-optimal sensor placement for linear inverse problems," *IEEE Trans. Signal Process.*, vol. 62, no. 5, pp. 1135–1146, Mar. 2014.
[6] C. Jiang, Y. C. Soh, and H. Li, "Sensor placement by maximal projection on minimum eigenspace for linear inverse problems," *IEEE Trans. Signal Process.*, vol. 64, no. 21, pp. 5595–5610, Nov. 2016.
[7] J. Wang and A. Yarovoy, "Sampling design of synthetic volume arrays for three-dimensional microwave imaging," *IEEE Trans. Comput. Imag.*, vol. 4, no. 4, pp. 648–660, Dec. 2018.
[8] A. Capozzoli, C. Curcio, and A. Liseno, "Singular value optimization in inverse electromagnetic scattering," *IEEE Antennas Wireless Propag. Lett.*, vol. 16, pp. 1094–1097, 2017.
[9] R. Piestun and D. A. B. Miller, "Electromagnetic degrees of freedom of an optical system," *J. Opt. Soc. Amer. A*, vol. 17, no. 5, pp. 892–902, 2000.
[10] R. Solimene, M. A. Maisto, G. Romeo, and R. Pierri, "On the singular spectrum of the radiation operator for multiple and extended observation domains," *Int. J. Antennas Propag.*, vol. 2013, Dec. 2013, Art. no. 585238.
[11] F. Soldovieri, R. Solimene, and F. Ahmad, "Sparse tomographic inverse scattering approach for through-the-wall radar imaging," *IEEE Trans. Instrum. Meas.*, vol. 61, no. 12, pp. 3340–3350, Dec. 2012.
[12] J. M. Lopez-Sanchez and J. Fortuny-Guasch, "3-D radar imaging using range migration techniques," *IEEE Trans. Antennas Propag.*, vol. 48, no. 5, pp. 728–737, May 2000.
[13] M. Soumekh, "A system model and inversion for synthetic aperture radar imaging," *IEEE Trans. Image Process.*, vol. 1, no. 1, pp. 64–76, Jan. 1992.
[14] S. Soumekh, "Depth-focused interior echo imaging," *IEEE Trans. Image Process.*, vol. 8, no. 11, pp. 1608–1618, Nov. 1999.

[15] J. Fortuny-Guasch and J. M. Lopez-Sanchez, "Extension of the 3-D range migration algorithm to cylindrical and spherical scanning geometries," *IEEE Trans. Antennas Propag.*, vol. 49, no. 10, pp. 1434–1444, Oct. 2001.

[16] T. Sakamoto, T. Sato, P. J. Aubry, and A. G. Yarovoy, "Ultra-wideband radar imaging using a hybrid of kirchhoff migration and Stolt F-K migration with an inverse boundary scattering transform," *IEEE Trans. Antennas Propag.*, vol. 63, no. 8, pp. 3502–3512, Aug. 2015.

[17] R. Solimene *et al.*, "SAR imaging algorithms and some unconventional applications: A unified mathematical overview," *IEEE Signal Process. Mag.*, vol. 31, no. 4, pp. 90–98, Jul. 2014.

[18] A. J. Devaney, *Mathematical Foundations of Imaging, Tomography and Wavefield Inversion*. Cambridge, U.K.: Cambridge Univ. Press, 2012.

[19] J. Fortuny-Guasch, "A novel 3-D subsurface radar imaging technique," *IEEE Trans. Geosci. Remote Sens.*, vol. 40, no. 2, pp. 443–452, Feb. 2002.

[20] G. Gilmore, I. Jeffry, and J. Lo Vetri, "Derivation and comparison of SAR and frequency-wavenumber migration within a common inverse scalar wave problem formulation," *IEEE Trans. Geosci. Remote Sens.*, vol. 44, no. 6, pp. 1454–1461, Jun. 2006.

[21] D. Cassereau and M. Fink, "Time-reversal of ultrasonic fields—Part III: Theory of the closed time-reversal cavity," *IEEE Trans. Ultrason., Ferroelect., Freq. Control*, vol. 39, no. 5, pp. 579–592, Sep. 1992.

[22] X. Zhuge, A. G. Yarovoy, T. Savelyev, and L. Ligthart, "Modified Kirchhoff migration for UWB MIMO array-based radar imaging," *IEEE Trans. Geosci. Remote Sens.*, vol. 48, no. 6, pp. 2692–2703, Jun. 2010.

[23] D. G. Dudley, T. M. Habashy, and E. Wolf, "Linear inverse problems in wave motion: Nonsymmetric first-kind integral equations," *IEEE Trans. Antennas Propag.*, vol. 48, no. 10, pp. 1607–1617, Oct. 2000.

[24] M. A. Maisto, R. Solimene, and R. Pierri, "Resolution limits in inverse source problem for strip currents not in Fresnel zone," *J. Opt. Soc. Amer. A*, vol. 36, no. 5, pp. 826–833, 2019.

[25] M. A. Maisto, R. Solimene and R. Pierri, "Depth resolution in strip current reconstructions in near non-reactive zone," *J. Opt. Soc. Amer. A*, vol. 36, no. 6, pp. 975–982, 2019.

[26] M. Cheney and R. J. Bonneau, "Imaging that exploits multipath scattering from point scatterers," *Inverse Problems*, vol. 20, no. 5, pp. 1691–1711, 2004.

[27] M. A. Maisto, R. Solimene, and R. Pierri, "Transverse resolution in microwave imaging for strip objects Buried in a half-space medium," *Progr. Electrom. Res. M*, vol. 88, pp. 145–157, 2020.

[28] F. Li, Q. H. Liu, and L.-P. Song, "Three-dimensional reconstruction of objects buried in layered media using Born and distorted Born iterative methods," *IEEE Geosci. Remote Sens. Lett.*, vol. 1, no. 2, pp. 107–111, Apr. 2004.

[29] L.-P. Song and Q. H. Liu, "Fast three-dimensional electromagnetic nonlinear inversion in layered media with a novel scattering approximation," *Inverse Problems*, vol. 20, no. 6, pp. 171–194, 2004.